

Research article

## Numerical characterisation of one-step and three-step solar air heating collectors used for cocoa bean solar drying

Elder Mendoza Orbegoso <sup>a,\*</sup>, Rafael Saavedra <sup>a</sup>, Daniel Marcelo <sup>a</sup>, Raúl La Madrid <sup>b</sup>

<sup>a</sup> Departamento de Ingeniería Mecánica Eléctrica, Universidad de Piura, Piura, Peru

<sup>b</sup> Departamento de Ciencias de la Ingeniería, Universidad de Piura, Piura, Peru

### ARTICLE INFO

**Article history:**

Received 27 January 2017

Received in revised form

21 June 2017

Accepted 6 July 2017

Available online 17 July 2017

**Keywords:**

Solar air heating collector

Computational fluid dynamics

Thermal efficiency

Discrete ordinates model

### ABSTRACT

In the northern coastal and jungle areas of Peru, cocoa beans are dried using artisan methods, such as direct exposure to sunlight. This traditional process is time intensive, leading to a reduction in productivity and, therefore, delays in delivery times. The present study was intended to numerically characterise the thermal behaviour of three configurations of solar air heating collectors in order to determine which demonstrated the best thermal performance under several controlled operating conditions. For this purpose, a computational fluid dynamics model was developed to describe the simultaneous convective and radiative heat transfer phenomena under several operation conditions.

The constructed computational fluid dynamics model was firstly validated through comparison with the data measurements of a one-step solar air heating collector. We then simulated two further three-step solar air heating collectors in order to identify which demonstrated the best thermal performance in terms of outlet air temperature and thermal efficiency. The numerical results show that under the same solar irradiation area of exposition and operating conditions, the three-step solar air heating collector with the collector plate mounted between the second and third channels was 67% more thermally efficient compared to the one-step solar air heating collector. This is because the air exposition with the surface of the collector plate for the three-step solar air heating collector former device was twice than the one-step solar air heating collector.

© 2017 Elsevier Ltd. All rights reserved.

### 1. Introduction

Cocoa beans are seeds from the fruit of cocoa trees (*Theobroma cacao*). Cocoa tree plantations grow naturally in tropical areas of Central and South America. The seeds comprise the raw material for the production of cocoa powder, cocoa butter and chocolate. It is essential that cocoa beans pass through fermentation and drying processes in order to transform into dry cocoa beans.

In the northern coastal and jungle areas of Peru in summer conditions, both the fermentation and drying processes require up to 12 days in order to produce the final product ready for exportation to European markets. Due to the absence of process technology, the cocoa transformation is carried out using artisanal methods. The drying of cocoa beans is completed through direct

exposure to sunlight. While fermentation takes around four days, the traditional process of drying cocoa beans takes approximately seven to eight days, creating bottlenecks in the continuous production of dry cocoa, which results in the creation of down times and, consequently, reductions in productivity and delays in delivery times.

It is for this reason that Peruvian government agencies are promoting researches and technological innovations that aim to solve this problem. Part of those researches include the development of prototypes for an indirect air solar dryer (IASD) that allows cocoa beans to be dried at temperatures lower than 60 °C in order to avoid poor quality beans with a strong acidic flavour, a weak "chocolate" flavour and the presence of other off-flavours. Such equipment is composed of a solar air heating collector (SAHC) connected to a drying chamber (DC). This solar dryer must be able to dry cocoa in the shortest time in order to be sufficiently resilient to efficiently operate under several operating conditions.

In connection with this study, there is a need to ascertain the geometrical and physical configuration of a SAHC that allows the maximum use of the sun's thermal energy in order to meet the

\* Corresponding author.

E-mail addresses: [eldermendoza\\_24@hotmail.com](mailto:eldermendoza_24@hotmail.com) (E.M. Orbegoso), [rafael.saavedra@udep.pe](mailto:rafael.saavedra@udep.pe) (R. Saavedra), [daniel.marcelo@udep.pe](mailto:daniel.marcelo@udep.pe) (D. Marcelo), [raul.lamadrid@udep.pe](mailto:raul.lamadrid@udep.pe) (R. La Madrid).

requirements needed for drying 100 kg cocoa in a maximum period of seven days. To this end, it is necessary to use numerical tools in order to describe with a high degree of precision the complex phenomena related to the drying process, such as natural and forced convection in a turbulent regime and their coupling with thermal radiation, etc., where their exact description and characterisation are not yet fully understood.

In this work, a computational fluid dynamics (CFD)-based model was developed in order to numerically characterise the thermal performance of SAHCs submitted under controllable operating conditions. This CFD model was employed for three types of SAHCs in order to identify the geometric and physical parameters that affect the collectors' thermal performance in terms of temperature, heat transfer and thermal efficiency. The results of the numerical simulations are extremely important in the pre-design stage because access to such information allows individuals to understand which SAHCs have the highest thermal energy efficiency and temperatures in accordance with exporters so they can obtain a highly efficient IASD capable of producing high-quality dried cocoa beans.

### 1.1. Bibliographical review

Studies over the last 25 years have designed and analysed SAHCs with the purpose of increasing the maximum utilisation of the sun's thermal energy. Leon and Kumar (2007) developed a mathematical model that reproduced the thermal performance of an unglazed transpired one-step SAHC under a wide range of geometrical and operating conditions. The modelling results were studied in order to predict the parameters such as porosity, airflow and irradiation, etc., that influence the thermal performance of such equipment. The results of this mathematical modelling determined that this SAHC had greater thermal efficiency than a conventional model. Moreover, the study demonstrated that airflow and the plate's separation greatly affect heat transfer effectiveness and efficiency. It is worth to emphasize that this type of SAHC is mainly used in ventilation systems but it was not found not in crop drying applications.

Using experimental and numerical approaches, Peng et al. (2010) investigated the thermal performance of a one-step SAHC with 27 pinned collector plates using several configurations of pin spacing and height. The objective of this research was to determine the specific plate collector configuration that operated with the best thermal performance. The results of this investigation showed that the plate collector with the longest and most concentrated pin arrangement produced the best heat transfer performance. Although this kind of pinned plate one-step SAHC provided an excellent thermal performance compared to a flat plate one-step SAHC, it has high construction demands associated with the high costs of its implementation on a commercial scale.

Amanlou and Zomorodian (2010) designed, constructed and evaluated a new cabinet dryer with a side-mounted plenum chamber in order to obtain a uniform distribution of drying airflow and temperature and produce the best overall operating conditions. To this end, seven different geometries of cabinet dryer were considered and experimental and numerical studies were performed. A comparison between experimental and numerical (extracted from CFD analysis) data revealed very good correlation between the drying air temperature and the air velocity in the drying chamber. Although this type of solar air dryer is very useful for crop drying, it lacks versatility in air drying temperature control, compromising the quality of the dried cocoa beans.

Kumar et al. (2012) developed a CFD model to simulate coupled heat and mass transfer during the convective drying of fruits to investigate several drying empirical models. This CFD model was

implemented in order to predict temperature and moisture distributions inside food during drying. The simulated results were compared with experimental data from the literature and the authors found a good level of agreement between both approaches. The development and use of CFD-based models are the most appropriate numerical approach for the design and analysis of solar air heating devices such as SAHCs.

Singh and Kumar (2012) developed numerical and experimental studies related to the steady state operation of three types of air solar dryers (direct, indirect and mixed) coupled with a one-step SAHC under controllable operating conditions such as irradiation and airflow. Both approaches yielded excellent agreements, which, in turn, allowed the authors to generate heat transfer correlations according to dimensionless parameters. The results obtained by the authors showed that the temperature gradient and airflow are parameters that strongly influence the thermal performance of such SAHCs. Consequently, these parameters must be taken into account in the design of SAHCs.

VijayaVenkataRaman et al. (2012) produced a bibliographical review of several air solar dryer designs, and their review takes into consideration design and operational parameters. In this review the authors considered as criteria: (i) the status of solar dryers with regard to developing countries; (ii) the design, development and performance evaluation of several types of solar dryers; (iii) the description of several types of dryers, such as natural convection and forced convection dryers, direct- and indirect-type dryers, integral dryers, greenhouse dryers, cabinet dryers, tunnel dryers and mixed mode dryers, which were reviewed in terms of their design and performance; (iv) solar drying technologies that facilitate the drying of crops in off-sunshine hours; and (v) solar dryers designed specifically for a particular crop, such as grain dryers, grape dryers, onion dryers and potato dryers, etc.

Jain and Tewari (2015) produced an experimental study related to the operation of an indirect solar dryer with storage material. In this work, the air temperatures at different positions of SAHCs and drying chambers were measured. According to the results obtained for drying mint, the study showed that between 7:00 and 23:00 h, the relative humidity in the drying chambers was lower than the environmental humidity. This was due to the presence of the storage material installed within the drying chamber. So, the presence of storage material is vital in the design of the SAHC for drying cocoa beans because it reduces undesirable high temperatures, storing thermal energy that will be released at intervals after sunset.

Bennamoun et al. (2015) studied the behaviour of peeled and unpeeled cherry tomatoes during forced convective drying. For this purpose, they used imaging techniques and analysis in order to adequately follow the variation of the volume during the convective drying of a single cherry tomato. The authors concluded that the shrinkage showed a linear decrease in the dimensionless volume as the moisture content decreased. The influence of the air temperature on the drying curves was also clearly identified. High temperatures caused a reduction in the drying time, as well as an increase in the moisture diffusion coefficient. The drying time for the unpeeled tomato was dramatically higher than that for the peeled tomato.

Chauhan et al. (2015) produced a review focusing on the application of CFD software in solar drying systems. The authors noted that the application of CFD software is very important for predicting the thermal performance of different kinds of solar drying systems. They also noted that this kind of tool is useful for predicting crop temperature, moisture content and the drying rate of crops, and they concluded that CFD can be used for the analysis of airflow and temperature distribution.

Fudholi et al. (2015) reviewed the design and performance of

different types of commercial scale solar drying systems with air-based solar collectors established in Malaysia. For this purpose, the performance of various solar air systems were summarised in detail. The authors examined thermal and drying performance indices such as drying time, evaporative capacity and drying efficiencies. The authors also reviewed the energy-exergy-environment-economic indices and their importance in the design and analysis of commercial scale solar drying systems.

Recently Sun et al. (2016) conducted an experimental and numerical study on the characterisation of a two-step SAHC with an intermediate collector plate (coflow). This study estimated the fluid dynamic and thermal behaviour of this SAHC when submitted to controllable operating conditions such as irradiation and mass flow. Both numerical and experimental results were in agreement, where different outlet temperature and efficiency results from both approaches did not exceed 1%. Moreover, the theoretical results determined that the thermal fluid behaviour of this intermediate collector plate SAHC is similar to most flat-type SAHCs. That is, as the outlet airflow was augmented, thermal efficiency increased and the outlet air temperature decreased. This behaviour is of paramount importance in the design and analysis of SAHCs for cocoa bean drying because the maximum mass-flow operation can be estimated in a situation of maximum irradiance in order to avoid temperatures higher than those allowed for good-quality dried cocoa beans.

## 1.2. Mathematical formulation

Sophisticated models have been used to describe the fluid dynamics and thermal behaviour of physical components involved in the drying process. In this way, CFD modelling considers the transport equations of mass, momentum and energy. These equations, coupled with the discrete ordinates model (DOM) and the standard  $\kappa-\omega$ , allow us to numerically describe the steady state operation of SAHCs submitted to several ranges of operating conditions.

The operation of the SAHC can be described by the solution of a set of equations and mathematical models that represent the fluid dynamic and thermal behaviour of the air that enters the collector, as well as its interactions with the device's solid elements.

### 1.2.1. Transport equations

Under the Reynolds Averaged Navier-Stokes (RANS) approach, the transport equations of mass, momentum and energy for a Newtonian fluid in steady state and turbulent flow are defined under the differential approach, Eulerian framework and indicial notation as:

$$\frac{\partial \bar{p}\tilde{u}_j}{\partial x_j} = 0 \quad (1)$$

$$\begin{aligned} \frac{\partial \bar{p}\tilde{u}_j\tilde{u}_i}{\partial x_i} &= -\frac{\partial \bar{p}}{\partial x_i} + (\bar{p} - \rho_{ref})g_i + \frac{\partial}{\partial x_j} \left[ \mu \left( \frac{\partial \tilde{u}_i}{\partial x_j} + \frac{\partial \tilde{u}_j}{\partial x_i} \right) \right. \\ &\quad \left. - \frac{2}{3} \mu \left( \frac{\partial \tilde{u}_k}{\partial x_k} \right) \delta_{ij} \right] + \frac{\partial}{\partial x_j} \left( -\bar{\rho} \tilde{u}_j'' \tilde{u}_i'' \right) \end{aligned} \quad (2)$$

$$\frac{\partial \bar{p}\tilde{h}_t}{\partial t} + \frac{\partial \bar{p}\tilde{u}_j\tilde{h}_t}{\partial x_j} = \frac{\partial}{\partial x_j} \left[ \frac{\mu}{Pr} \left( \frac{\partial \tilde{h}_t}{\partial x_j} \right) \right] + \frac{\partial}{\partial x_j} \left( -\bar{\rho} \tilde{u}_j'' \tilde{h}_t'' \right) + \bar{S}_r \quad (3)$$

where

$$-\bar{\rho} \tilde{u}_j'' \tilde{u}_i'' = \mu_t \left( \frac{\partial \tilde{u}_i}{\partial x_j} + \frac{\partial \tilde{u}_j}{\partial x_i} \right) - \frac{2}{3} \left( \bar{\rho} \kappa + \mu_t \frac{\partial \tilde{u}_k}{\partial x_k} \right) \delta_{ij} \quad (4)$$

$$-\bar{\rho} \tilde{u}_j'' \tilde{h}_t'' = \frac{\mu_t}{\sigma_h} \left( \frac{\partial \tilde{h}_t}{\partial x_j} \right) \quad (5)$$

$$\kappa = \frac{1}{2} \bar{u}_i \bar{u}_i \quad (6)$$

In this set of equations,  $\tilde{u}_i$  and  $\tilde{h}_t$  represent the Favre average of the velocity and total enthalpy of the fluid flow.

As can be seen in Eq. (3), the energy contribution due to viscous dissipation and turbulent dissipation are not taken into consideration because both terms are negligible in comparison to the thermal diffusion, the turbulent flux of enthalpy and the source term due to thermal radiation. Moreover,  $-\bar{\rho} \tilde{u}_j'' \tilde{u}_i''$  and  $-\bar{\rho} \tilde{u}_j'' \tilde{h}_t''$  of Eqs. (2) and (3) correspond to the respective Reynolds stresses and the turbulent flux of enthalpy, which are modelled according to the Boussinesq and gradient hypothesis, respectively (Schlichting and Gersten, 2000). In Eq. (2),  $\bar{p}$  and  $\rho_{ref}$  correspond to the average and reference density, while  $\mu$  is the dynamic viscosity of the fluid. In Eq. (3),  $Pr$  is the Prandtl number, while  $\bar{S}_r$  is the energy equation source term related to thermal radiation. Finally, in Eqs. (4)–(6),  $\mu_t$  is the turbulent viscosity,  $\sigma_h$  is the turbulent Prandtl number and  $\kappa$  is the turbulent kinetic energy that is characterised by the root mean square of velocity fluctuations. It should be noted that this set of equations is only valid for subsonic flows with a low Mach number,  $Ma = u/c < < 1$ , where the energy contribution due to temporal pressure variations is negligible (Schlichting and Gersten, 2000).

For a solid body without motion, the energy conservation equation corresponds to the following formulation (ANSYS, 2012):

$$\frac{\partial \rho_s h_s}{\partial t} = \frac{\partial}{\partial x_j} \left[ k_s \left( \frac{\partial T_s}{\partial x_j} \right) \right] + S_s \quad (7)$$

where  $\rho_s$  is the solid density,  $h_s$  is the solid enthalpy,  $k_s$  is the solid thermal conductivity and  $S_s$  is the source term of the solid associated with the phenomena as electrical heating, thermal radiation, etc.

### 1.2.2. The $\kappa-\omega$ RANS turbulence model

The turbulence model  $\kappa-\omega$  corresponds to a set of empirical formulations comprised of two differential equations coupled with additional algebraic equations that allow the closure of these equations. These differential equations describe the transport of the turbulent kinetic energy,  $\kappa$ , and the vortex transport generated by turbulence,  $\omega$ , that is diminished due to the turbulent dissipation rate,  $\varepsilon$ . This model has evolved over time with the addition and subtraction constants and functions that describe the production and destruction of  $\kappa$  and  $\omega$ , resulting in a model that predicts internal turbulent flows with good precision. In this paper, the  $\kappa-\omega$  model proposed by Wilcox (2008) is described by the following formulations:

$$\frac{\partial \bar{\rho} \kappa}{\partial t} + \frac{\partial \bar{\rho} \tilde{u}_j \kappa}{\partial x_j} = \frac{\partial}{\partial x_j} \left[ \left( \mu + \frac{\mu_t}{\sigma_\kappa} \right) \frac{\partial \kappa}{\partial x_j} \right] + P_\kappa - Y_\kappa + P_{\kappa b} \quad (8)$$

$$\frac{\partial \bar{p}\omega}{\partial t} + \frac{\partial \bar{p}\tilde{\mu}_j\omega}{\partial x_j} = \frac{\partial}{\partial x_j} \left[ \left( \mu + \frac{\mu_t}{\sigma_\omega} \right) \frac{\partial \omega}{\partial x_j} \right] + G_\omega - Y_\omega + P_{\omega b} \quad (9)$$

where the eddy viscosity in the  $\kappa$ - $\omega$  model is defined as:

$$\mu_t = \frac{\bar{p}\kappa}{\omega} \quad (10)$$

In Eqs. (8) and (9),  $P_\kappa$  and  $G_\omega$  correspond to the terms associated with the production of turbulent kinetic energy and turbulent frequency, while  $Y_\kappa$  and  $Y_\omega$  indicate the destruction of turbulent kinetic energy and turbulent frequency. The Prandtl numbers, associated with the turbulent kinetic energy and turbulent frequency, are often defined by  $\sigma_\kappa$  and  $\sigma_\omega$ , which are the same as those assumed by Wilcox (2008), that is to say, equal to 2.

### 1.2.3. The thermal radiation DOM

For a medium, fluid or solid, the thermal radiation contribution in the energy transport equations [Eqs. (3) and (7)] is taken into account by the source terms whose values depend on the incident radiation,  $G$ , defined as (Modest, 2003):

$$G(\vec{r}, \vec{s}) = \int_0^{4\pi} i(\vec{r}, \vec{s}') d\Omega \quad (11)$$

On the other hand, the source terms associated with thermal radiation for a semi-transparent participant fluid,  $\bar{S}_r$  and gray semi-transparent solid,  $S_s$ , are expressed as (Orbegoso et al., 2015):

$$\bar{S}_r = -\nabla \cdot \bar{q}_r = \nabla \cdot (\bar{T} \nabla \bar{G}) \equiv \bar{a}_g \bar{G} - 4\bar{a}_g \sigma \bar{T}^4 \quad (12)$$

$$S_s = -\nabla \cdot \bar{q}_r = \nabla \cdot (\bar{T} \nabla G) \equiv a_s G_s - 4a_s \sigma T^4 \quad (13)$$

where  $\sigma$  is the Stefan-Boltzman constant equal to  $5.670 \times 10^{-8}$  W/m<sup>2</sup>K<sup>4</sup>,  $\bar{a}_g$  and  $a_s$  are the overall absorption coefficients for fluid and solid medium,  $\bar{G}$  is the average incident radiation over a fluid medium,  $G_s$  is the incident radiation over a solid medium,  $\bar{T}$  is the Reynolds averaged temperature of the fluid medium and  $T$  is the temperature of the semi-transparent solid medium. It should be emphasised that Eq. (12) is only valid when the correlations between (i) temperature and overall absorption coefficient fluctuations and (ii) incident radiation and overall absorption coefficient fluctuations are both negligible.

Producing the solutions for Eqs. (12) and (13) requires previous knowledge of the overall absorption coefficient, the absolute temperature and the incident radiation. For the thermal numerical characterisation of SAHCs that use homogeneous materials and operate at low temperature ranges it can be assumed, without loss of accuracy, that the absorption coefficient for a solid medium or a fluid medium is constant.

In order to determine the incident radiation, Eq. (11) must be resolved. Note that the radiation intensity,  $i$ , is a dependent variable that, in a quasi steady state, is calculated by solving the radiant transfer equation (RTE) that, in its global form, is expressed as (Modest, 2003):

$$\frac{di(\vec{r}, \vec{s})}{ds} = -(a + \sigma_s) i(\vec{r}, \vec{s}) + an^2 \frac{\sigma T^4}{\pi} + \frac{\sigma_s}{4\pi} \int_0^{4\pi} i(\vec{r}, \vec{s}') \Phi(\vec{s}, \vec{s}') d\Omega' \quad (14)$$

In this equation,  $i(\vec{r}, \vec{s})$  is the radiation intensity of the global

radiant energy of a small beam travelling through a medium at a given location indicated by an  $\vec{r}$  position in the  $\vec{s}$  direction,  $a$  is the global absorption coefficient that might be  $a_s$  and  $\bar{a}_g$  depending on whether the medium is solid or fluid, respectively,  $\sigma_s$  is the scattering coefficient of the medium, while  $n^2$  is the refractive index,  $\Phi(\vec{s}, \vec{s}')$  is the scattering phase function and  $\Omega'$  is the solid angle variable.

In Eq. (14), the first term on the right-hand side describes the reduction of the radiation intensity along a beam direction,  $\vec{s}$ , due to absorption and scattering in other directions. The second term on the right-hand side is related to increases in radiation intensity due to thermal emission by the medium and the last term is relevant only if the participant media scatters radiation. In this term, the phase function,  $\Phi(\vec{s}, \vec{s}')$  describes the probability of a beam that comes from an  $\vec{s}'$  direction that scatters to an  $\vec{s}$  direction.

For the operation of the SAHC, the scattering phenomena can be neglected assuming that (i) solid materials are homogeneous and isotropic and (ii) the airflow does not drag suspended dust particles or droplets of water. So, the RTE [Eq. (14)] can be simplified to (ANSYS, 2012):

$$\frac{d i(\vec{r}, \vec{s})}{ds} = -a \left[ i(\vec{r}, \vec{s}) + \frac{\sigma T^4}{\pi} \right] \quad (15)$$

Over time, several radiant models have been developed to solve the RTE. These studies include various analytical approaches and numerical methods. A very sophisticated model that numerically solves this equation is the DOM, which discretises the RTE in a finite number of solid angles, each associated with a direction vector,  $\vec{s}$ , and its corresponding weight factor. This model was initially proposed by Chandrasekhar (1960) for atmospheric and astrophysical problems. The model is currently used for several problems involving thermal radiation and is commonly applied for the numerical description of turbulent combustion of sooting fuels (Orbegoso et al., 2015). The model's computational cost is high, even for small numbers of angular discretisation, so it requires high-performance computers in terms of processing speed and memory storage.

### 1.2.4. Solar collector thermal efficiency

The thermal efficiency of a solar collector is based on the heat balance between the solar radiation energy, the energy absorbed by the air stream and the energy lost to the environment. The thermal energy balance of a solar collector can be described as:

$$IA_c(\tau\alpha) = \dot{Q}_{abs} + \dot{Q}_{lost} \quad (16)$$

where  $I$  is the solar irradiation,  $A_c$  is the surface area of the collector plate,  $(\tau\alpha)$  is the product of solar transmittance and absorptance,  $\dot{Q}_{abs}$  is the thermal power absorbed by the air stream and  $\dot{Q}_{lost}$  is the thermal power lost to the environment.

Based on the above equation, the thermal efficiency of the solar collector,  $\eta_T$ , is obtained by the following formula:

$$\eta_T = \frac{\dot{Q}_{abs}}{IA_c} \quad (17)$$

that defines the ratio of the solar radiation energy that is converted into useful heat.

## 2. Materials and methods

The first step in any analysis or design process using CFD tools is the definition of the computational domain, i.e., the creation of the

geometry of the spatial region where the study of the flow will be made. This domain is then discretised by a finite set of control volumes. The flow characteristic, which is described in each control volume, is solved numerically in a manner that determines the discrete values of velocity, pressure, temperature and other transport parameters.

The precision of a CFD solution is strongly influenced by the number of finite volumes in which the computational domain was discretised. While, in general, the increase in the number of finite volumes improves the accuracy of CFD results, the type of mesh and the order of the numerical method also influence the final solution. It is worth emphasising that the application of these factors is limited by computational capacity in terms of the processing and memory storage of the hardware where the simulation will be performed.

### 2.1. Description of experimental setup used by Singh and Kumar (2012)

As shown in Fig. 1, the SAHC chosen for simulation was developed and experimentally measured by [Singh and Kumar \(2012\)](#). This device is a one-step plate collector whose effective surface is  $0.414 \text{ m}^2$ , distributed by  $0.92 \times 0.45 \text{ m}$  in its length and width and inclined to  $15^\circ$  from the horizontal. Further, 4 mm thick glass covers the top of the SAHC in order to isolate the working air from the ambient air. This glass cover is placed 20 mm above the 1 mm thick aluminium collector plate. This collector plate is settled on glass wool with a 50 mm thick medium of thermal insulation. All the elements described above are set on a wooden cabinet.

Experiments using this device were performed indoors in order to ensure experimental measures were under controllable operating conditions. To do this, the authors used a set of nine heating plates of  $0.05 \times 0.09 \text{ m}$  in size with 500 W each. Furthermore, an electric motor coupled to a centrifugal fan permitted the flow of air within from the fan to the collector via a transition piece.

Measurements of the thermal power of the collector plate as well air mass flow were conducted at steady state for four to six hours, collecting enough data with a high level of accuracy. The criteria used for the definition of the steady state were that, over a period of 10 min., the variation in the temperature measurements for each SAHC component did not exceed  $\pm 1\%$ . These experiments were repeated for a wide range of input data that covered

$300\text{--}800 \text{ W/m}^2$  of solar irradiation and 0.009 to 0.026 kg/s of air mass flow.

### 2.2. CFD modelling description

The simulation process began with the determination of the computational domain. It was decided to use only a portion (45 mm width) of the [Singh and Kumar \(2012\)](#) one-step SAHC in order to reduce the computational burden. This simplification was supported by the symmetry at the device's width, apart from the high width/height ratio of 22.5 in the "Air" subdomain cross-section region. Under both situations, the simulation of this one-step SAHC, considering the infinite parallel flat plate's configuration as the hypothesis, could be performed without an appreciable loss of precision.

[Fig. 2](#) shows the collector geometry where it can be seen that the computational domain is divided into four subdomains comprising the following collector elements: "Glass"; "Air"; "Plate"; and "Insulator". Once the computational domain is generated, it is discretised into hexahedral elements. The "Glass" and "Plate" subdomains are discretised with 88,000 and 40,000 elements, respectively. In addition, the "Air" subdomain is discretised into 250,000 hexahedral elements, whereas the "Insulator" domain is discretised into 160,000 elements.

The total number of elements that constitute the computational domain is 490,000 hexahedral elements, arranged in a manner so that a higher concentration of these are found in regions near the boundaries of the air with glass and plate, where the minimum cell size of the "Air" subdomain in the vicinity of glass and plate (in a normal direction) is 0.32 mm. This size assures a precise description of the turbulent boundary layer at low Reynolds numbers.

[Fig. 2](#) also shows in detail part of the discretisation results for the four subdomains. It is important to emphasise that the aspect ratio of the elements in the "Air" subdomain ranges from 1.40 at the core of the flow to 6.69 at the vicinity of glass and plate. These values are within those recommended by most CFD software.

The [Singh and Kumar](#) one-step SAHC setting up the simulation of the fluid dynamics and thermal behaviour of the computational domain is performed through the use of the ANSYS-Fluent software. This software takes into consideration the simultaneous thermal interaction of the four aforementioned subdomains. [Table 1](#) details the thermodynamic properties of the materials that

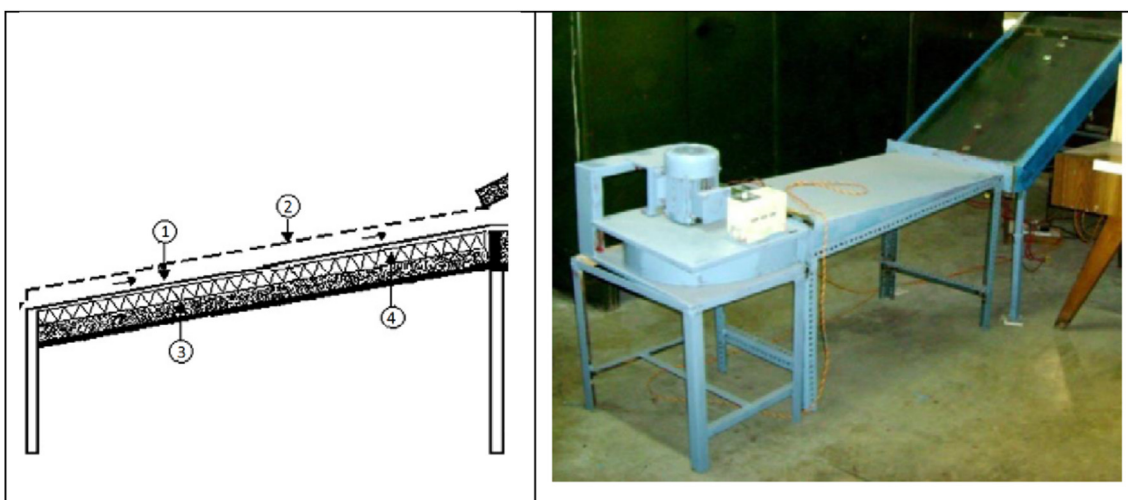


**Fig. 1.** Schematic (left) and photographic (right) images of the flat plate collector one-step with cover glass and aluminium collector plate: (1) channel; (2) glass cover; (3) thermal insulation; and (4) collector plate [Singh and Kumar \(2012\)](#).

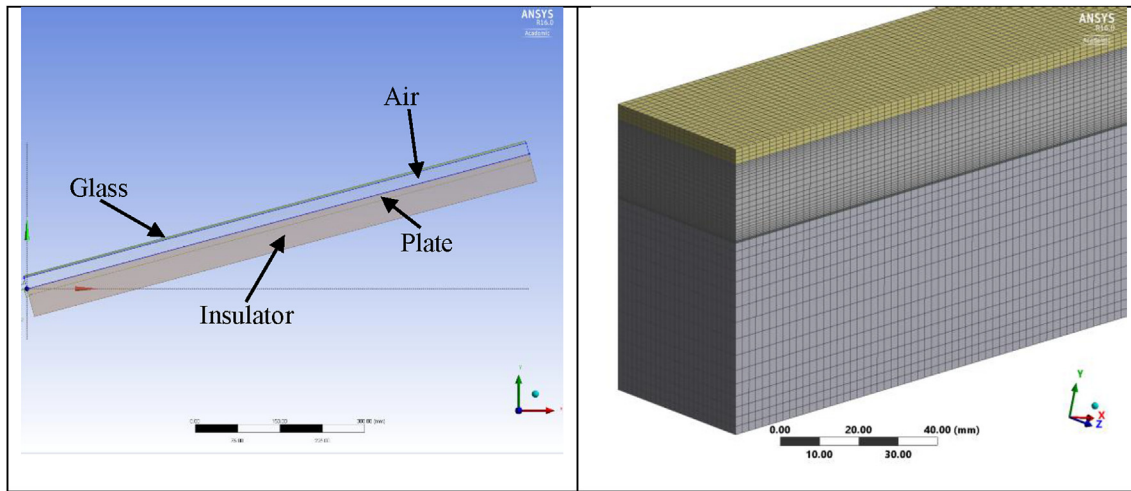


**Fig. 2.** Three-dimensional geometric configuration of the one-step SAHC computational domain (left) and its discretisation in hexahedral elements (right).

have been used as input data for numerical simulations. Note that the air density was adopted as an ideal gas:

$$p_{abs}/\rho_{air} = R_{air}T \quad (18)$$

where  $p$  is the absolute pressure,  $\rho_{air}$  is the air density,  $R_{air}$  is the air constant equal to 0.287 kJ/kg.K and  $T$  is the air temperature. The specific heat at constant pressure was understood as a temperature-dependent polynomial function taken from the ANSYS-Fluent database for air (ANSYS, 2012):

$$\begin{aligned} c_{p,air} = & 1161.482 - 2.368849T + 0.01485511T^2 - 5.034909 \\ & \times 10^{-5}T^3 + 9.928569 \times 10^{-8}T^4 - 1.111097 \times 10^{-10}T^5 \\ & + 6.540196 \times 10^{-14}T^6 - 1.573588 \times 10^{-17}T^7 \end{aligned} \quad (19)$$

Air viscosity was also considered as temperature dependent and it can be described according to the following Sutherland formulation:

$$\mu = \mu_0 \left( \frac{T}{T_0} \right)^{3/2} \frac{T_0 + S}{T + S} \quad (20)$$

where the reference viscosity,  $\mu_0$ , the reference temperature,  $T_0$ , and the effective temperature,  $S$ , are assumed equal to 1.716.10<sup>-5</sup> Pa s, 0.0399939 °C and –162.59 °C, respectively (ANSYS, 2012). The remainder properties were kept constant. It is worth noting that the air was considered in the simulation as a semi-transparent fluid with a very low absorption coefficient,  $a$ . The absorption coefficients for glass and plate were previously estimated using Beer's law (Modest, 2003) that relates transmissivity as an exponential function of the absorption coefficient. Moreover, it was considered that the fibreglass did not participate in the

radiation heat transfer phenomena.

The operating and boundary conditions are shown in Table 2. For the glass case, the sky temperature was assumed to be identical to the ambient temperature; b experimental measures of the one-step SAHC were performed in-house.

All the transport equations used for the SAHC simulation were discretised through the solution of the second order "up wind" scheme. In addition, convergence criteria were considered as: (i) root mean square residuals must be less than  $1 \times 10^{-6}$ ; (ii) imbalances in the conservation equations must be lower than 0.01%; and (iii) the variation in the step-by-step iteration in the fluid dynamics and thermal magnitudes as the mass flow averaged outlet velocity and temperature must be less than 0.1%.

### 3. Results and discussion

This section discusses the numerical results obtained in the application of the developed CFD model in order to describe the fluid dynamic and thermal performance of the SAHCs. For this purpose, three case studies were considered: (i) the validation of the CFD model with the experimental results of a one-step SAHC by Singh and Kumar (2012) under several operating conditions; (ii) the fluid dynamic and thermal analysis of the same one-step SAHC under the maximum air mass flow and maximum solar irradiance operating conditions; and (iii) a comparative thermal performance study of three different configurations of SAHCs submitted to the same operating conditions.

#### 3.1. Validation of CFD results with Singh and Kumar's (2012) measurements

The CFD numerical results compared with the experimental results are shown in Figs. 3 and 4 and Table 3. The results obtained

**Table 1**  
Thermal properties assigned to the subdomains of the computational domains.

Subdomain	Properties					
	Material	$\rho$ [kg/m <sup>3</sup> ]	$c_p$ [J/kg K]	$k$ [W/m K]	$\mu$ [Pa.s]	$a$ [1/m]
Glass	Glass	2500	750		1.4	
Air	Air	Ideal gas	Polynomial function	0.0242	Sutherland	5 0.0001
Plate	Aluminium	2719	871	202.4		2325.9
Isolator	Fibreglass	220	750	0.035		

**Table 2**

Operating and boundary conditions assigned to the computational domain.

Subdomain	Boundary	Boundary Condition
Glass	Ambient	$I = 300, 450, 600, 750, 800 \text{ W/m}^2$ $T_{amb}$ : According to Singh and Kumar's measurements (Singh and Kumar, 2012). $h_{ext}$ : 0.1–3.0 $\text{W/m}^2\text{K}$ (as $I$ linear interpolation function) $\epsilon_{glass,out} = 0.9$ , $T_{sky} = T_{amb}$ (in house condition) $\epsilon_{glass,int} = 0.9$
Air	Air subdomain Inlet	$\dot{m}_{air} = 0.009, 0.017, 0.026 \text{ kg/s}$ and natural convection $T_{air,inlet} =$ : According to Singh and Kumar's measurements (Singh and Kumar, 2012). $I_t = \sqrt{\frac{u_{k,0}''^2}{u_{k,0}}} = 0.01$ (low turbulent intensity) $p_{gauge} = 0 \text{ Pa}$
Plate	Outlet Glass subdomain Plate subdomain Air subdomain	$\epsilon_{glass,int} = 0.9$ $\epsilon_{plate,out} = 0.95$ $\epsilon_{plate,out} = 0.95$ $\epsilon_{plate,in} = 0$
Isolator	Insulator subdomain Plate subdomain Ambient	$\epsilon_{plate,in} = 0$ $T_{amb}$ : According to Singh and Kumar's measurements (Singh and Kumar, 2012). $h_{ext}$ : 0.1–3.0 $\text{W/m}^2\text{K}$ (as $I$ linear interpolation function) $\epsilon_{fiber,out} = 0$

by both approaches involve the average outlet air temperature and the average temperature of the collector plate. Both comparison parameters were performed at four operation air mass flow conditions (0.026, 0.017, 0.009 kg/s and “natural convection”) subjected to solar irradiation conditions that ranged from 300 to 800  $\text{W/m}^2$ .

With reference to Fig. 3 and Table 3, it can be seen that there is a good agreement among the average air temperatures obtained by both the CFD simulation and the experimental measurement approaches. In particular, the agreement of both approaches is better in the case of “high mass flow rates” (i.e., 0.026 and 0.017 kg/s) than in the case of “low mass flow rates” (i.e., 0.009 kg/s and “natural

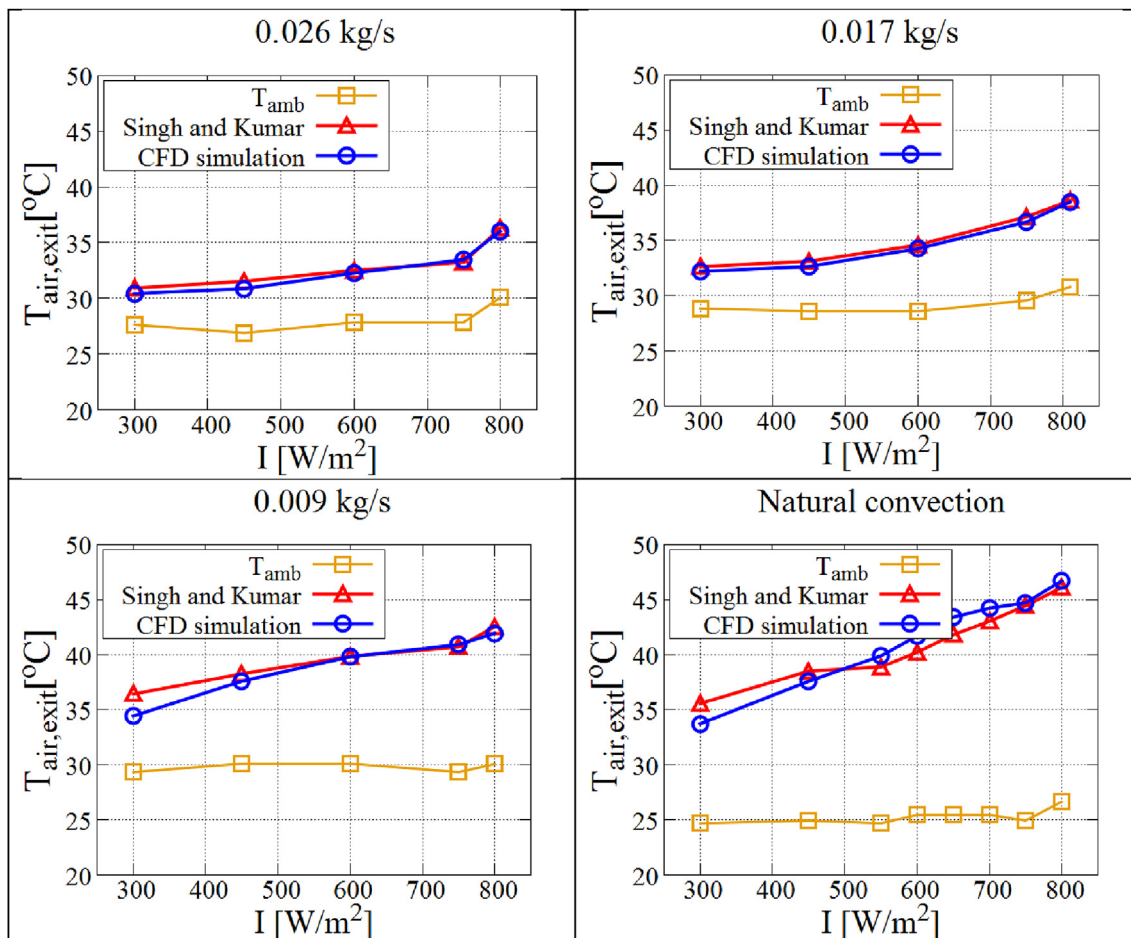
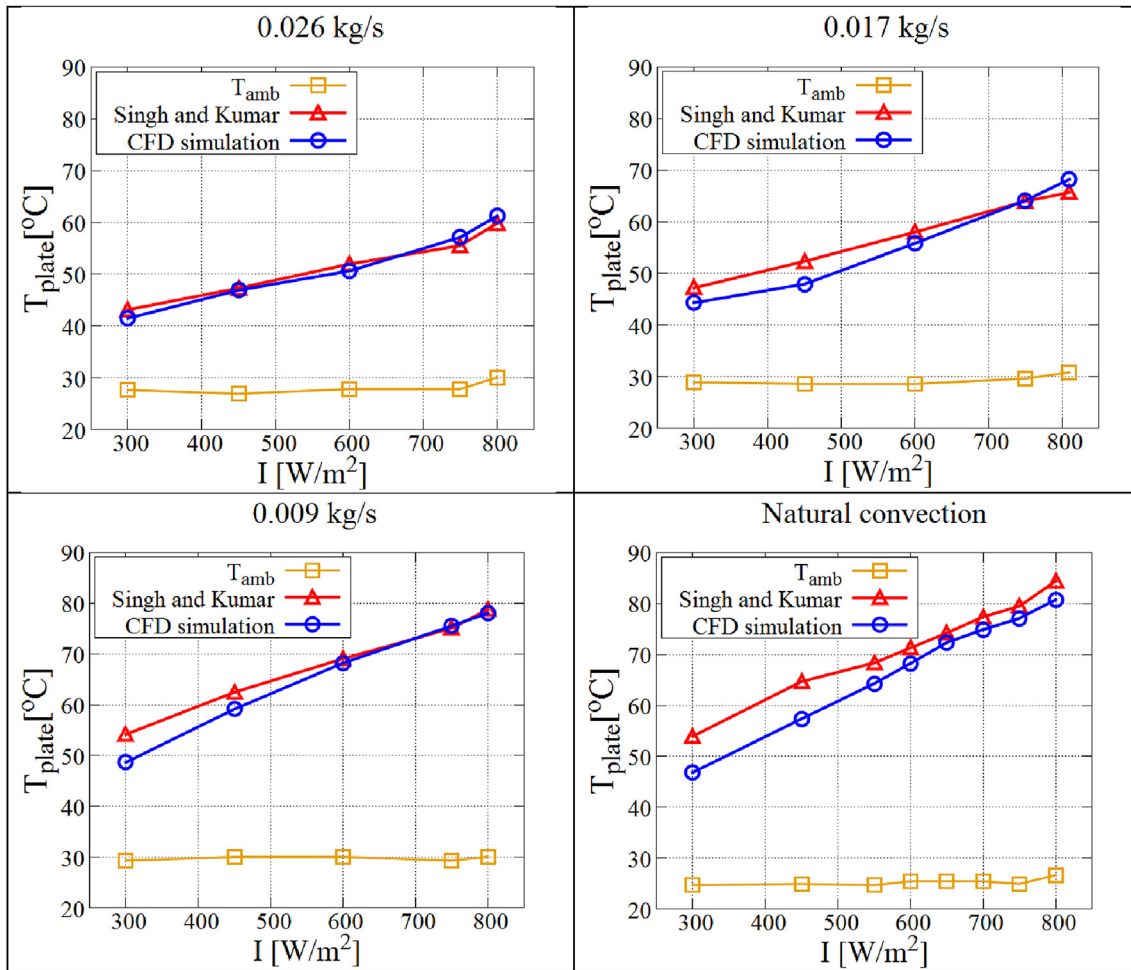


Fig. 3. Influence of the average air temperature at the SAHC's outlet with respect to solar irradiance. Comparison of CFD results with the Singh and Kumar (2012) experiments.



**Fig. 4.** Influence of the average temperature of the collector plate relative to the solar irradiance and for different mass flow rates.

convection"). It is presumed that this behaviour occurred because the flow in "high mass flow rates" is more uniform than "low mass flow regimes" as a result of forced convection that is more intense than natural convection. For internal flow regimes flowing in parallel plates and where natural convection exerts equal or greater influence than forced convection (ie.,  $Ri \geq 0.1$ ) (Turner, 1973), there can be flow and temperature oscillations due to natural convection, which becomes the most predominant phenomenon. These oscillations could generate the Rayleigh-Bernard instability (Bejan, 2013) when the Rayleigh number,  $Ra$ , overcomes the critical  $Ra_{CR} = 1708$ . In this situation, the airflow begins to contra-rotate. This phenomenon was observed in the "natural convection" mass flow rate case, but it is not shown in this work for the sake of brevity.

For "low flow mass rates", Fig. 3 and Table 3 demonstrate that the concordance is smaller as solar irradiance becomes weaker, reaching slight discrepancies that do not exceed 5.5%. It is presumed that such discrepancies, despite being low, are due to several factors that range from the sensitivity of the measuring instruments to a lack of specific information for establishing a perfect conditioning in the boundary conditions, such as the real values of rugosity, emissivity and transmissivity of the materials used in such a collector.

Fig. 4 and Table 3 show the comparison between the numerical

simulation and the experimental data obtained by Singh and Kumar (2012) concerning the average temperature of the collector plate. Note that for "high mass flow rates" (i.e., 0.026 and 0.017 kg/s), there is also a good agreement between the experimental and simulation results in most of the domain analysis where discrepancies do not exceed 10%; in fact, in most cases, they are below 5%.

For "low mass flow rates" (i.e., 0.09 kg/s and "natural convection"), numerical and experimental discrepancies with regard to the collector plate's average temperature are higher than those observed for "high mass flow rates".

In conclusion, the CFD model developed in this work had very good consistency with the experimental results (Singh and Kumar, 2012), which corresponds with the prediction of thermal parameters relating to the one-step SAHC's operation. This model will be used for the analysis of the fluid dynamic and thermal behaviour of such equipment, as well as for sizing the solar collector that will be used as a component of a solar dryer to be designed.

The numerical results describing the fluid dynamics and the thermal characteristics of Singh and Kumar's (2012) one-step SAHC under the conditions of maximum irradiance and high mass flow rate will be analysed in the following section. It is worth emphasizing that this is the case where forced convection prevails over natural convection.

**Table 3**

Comparison of results from CFD simulation experiments by Singh and Kumar (2012).

Irradiance $I [\text{W/m}^2]$	Amb. temp. $T_{\text{amb}} [\text{°C}]$	Temperature of the air at the outlet			Temperature of the plate		
		$T_{\text{air,exit}} [\text{°C}]$	Singh & Kumar	CFD simulation	% error	$T_{\text{plate}} [\text{°C}]$	Singh & Kumar
<b><math>\dot{m}_{\text{air}} = 0.026 \text{ kg/s}</math></b>							
300	<b>27.63</b>	30.93	30.44	1.6	43.15	41.49	<b>3.8</b>
450	<b>26.90</b>	31.54	30.88	<b>2.1</b>	47.31	46.92	0.8
600	<b>27.87</b>	32.52	32.28	0.7	51.96	50.63	2.6
750	<b>27.87</b>	33.25	33.49	0.7	55.50	57.10	2.9
800	<b>30.07</b>	36.31	36.03	0.7	59.78	61.20	2.4
<b><math>\dot{m}_{\text{air}} = 0.017 \text{ kg/s}</math></b>							
300	<b>28.85</b>	32.64	32.21	1.3	47.19	44.30	6.1
450	<b>28.61</b>	33.13	32.66	<b>1.4</b>	52.32	47.91	<b>8.4</b>
600	<b>28.61</b>	34.60	34.27	1.0	57.95	55.78	3.7
750	<b>29.58</b>	37.16	36.69	1.3	63.94	64.07	0.2
810	<b>30.81</b>	38.63	38.50	0.3	65.65	68.19	3.9
<b><math>\dot{m}_{\text{air}} = 0.009 \text{ kg/s}</math></b>							
300	<b>29.34</b>	36.43	34.43	<b>5.5</b>	54.16	48.67	<b>10.1</b>
450	<b>30.07</b>	38.26	37.60	1.7	62.47	59.13	5.3
600	<b>30.07</b>	39.85	39.81	0.1	69.07	68.22	1.2
750	<b>29.34</b>	40.71	40.91	0.5	75.06	75.53	0.6
800	<b>30.07</b>	42.54	41.94	1.4	78.73	78.04	0.9
<b>Natural convection</b>							
300	<b>24.69</b>	35.57	33.73	<b>5.2</b>	53.91	46.83	<b>13.1</b>
450	<b>24.94</b>	38.51	37.59	2.4	64.67	57.35	11.3
550	<b>24.69</b>	38.88	39.89	2.6	68.34	64.27	6.0
600	<b>25.43</b>	40.22	41.70	3.7	71.27	68.23	4.3
650	<b>25.43</b>	41.81	43.40	3.8	74.21	72.34	2.5
700	<b>25.43</b>	43.03	44.22	2.8	77.38	74.87	3.2
750	<b>24.94</b>	44.25	44.71	0.6	79.46	77.09	3.0
800	<b>26.16</b>	46.09	46.69	1.3	82.40	80.75	4.3

The bold numbers in the % error are the maximum percentage value.

### 3.2. Analysis of the one-step SAHC for the case of maximum irradiance and high air mass flow

This section discusses the fluid dynamic and thermal behaviour of the experimental one-step SAHC for the case in which this equipment is exposed to maximum irradiance (i.e.,  $800 \text{ W/m}^2$ ) and simultaneously operates a regime of high air mass flow (i.e.,  $0.026 \text{ kg/s}$ ). The operating point was chosen according to three criteria: (i) the condition of operation is when the collector has maximum energy exposure from the sun, i.e., clear sky, times between 12 and 14 h, in summer season, etc.; (ii) the collector operates at high thermal efficiencies; and (iii) the CFD simulation results are virtually identical to those displayed in Singh and Kumar's (2012) measurements, where disagreements are practically nonexistent.

The top of Fig. 5 shows the air velocity contours in the XY plane for the case of maximum irradiance (i.e.,  $800 \text{ W/m}^2$ ) and high mass airflow (i.e.,  $0.026 \text{ kg/s}$ ). As can be observed in this figure, the airflow enters the one-step SAHC with a uniform profile. Due to the presence of the inner walls of the glass cover and solar collector, the boundary layer grows downstream, retarding the axial flow at the inner walls and accelerating the center core of the flow until it reaches a position in which the velocity profile no longer changes.

The distance from the SAHC's entrance to the position where there is no change in the velocity profile is called the developing length,  $L_e$ , which in this case can be identified as a low Reynolds number regime ( $Re_D \approx 3200$ ), the turbulent developing length (applying  $L_e \approx 4.4D_h Re_D^{1/6}$ ) is approximately 340 mm or 0.37  $L$ , where  $L$  is the length of the one-step SAHC. When downstream in this last position, the flow is fully developed.

The bottom of Fig. 5 shows the velocity profiles at  $0.01L$ ,  $0.11L$ ,  $0.28L$ ,  $0.57L$  and  $0.85L$ . These velocity profiles indicate that at  $0.01L$ ,  $0.11L$  and  $0.28L$ , the turbulent flow is in the developing region whereas at positions  $0.57L$  and  $0.85L$ , the turbulent flow is fully

developed.

The air temperature contours along the interior of the solar collector are shown in Fig. 6. Note that in the SAHC inlet, the air temperature that enters at  $30.1 \text{ °C}$  increases in the lower region as a result of thermal energy transfer between the collector plate and the air. In addition, the air at the top region increases several Celsius degrees, ranging from  $30.1$  to  $33.4 \text{ °C}$ . This is because the cover glass does not contribute significantly to the heating of the air.

The bottom part of Fig. 6 shows the contours of the outlet air temperature. It is evident that the air leaves the one-step collector at non-uniform temperatures. In other words, high air temperatures up to  $63.3 \text{ °C}$  are observed near the collector plate whereas 40% of the air temperature is between  $30.1$  and  $33.4 \text{ °C}$ . This observation indicates that a large percentage of air does not carry significant warming.

Surface temperatures over the collector plate and the cover glass are shown in Fig. 7 in the case of the collector operating under maximum irradiance and maximum air mass flow. In the case of the collector plate, it can be seen that its surface temperature is not uniform; however, it has a temperature gradient along the airflow path, wherein temperatures of  $49.8 \text{ °C}$  are observed in the collector plate limited by the air inlet region. This temperature increases gradually along the airflow path, reaching a maximum of  $63.3 \text{ °C}$  in the region adjacent to the air near to the outlet collector.

An appreciable temperature gradient can be observed along the collector plate; even this component is composed of a thermally conductive material (aluminum). This is due to the one-step SAHC not having thermal storage material. On the contrary, the bottom of the collector plate is coupled to an insulating material such as fibreglass. The reason for this is that the collector plate absorbs most of the radiant energy from the sun, re-transferring to the air through the convection heat transfer mechanism. This heat transfer is greater in the initial transitional stages of the collector plate because the air that enters the solar collector with uniform velocity

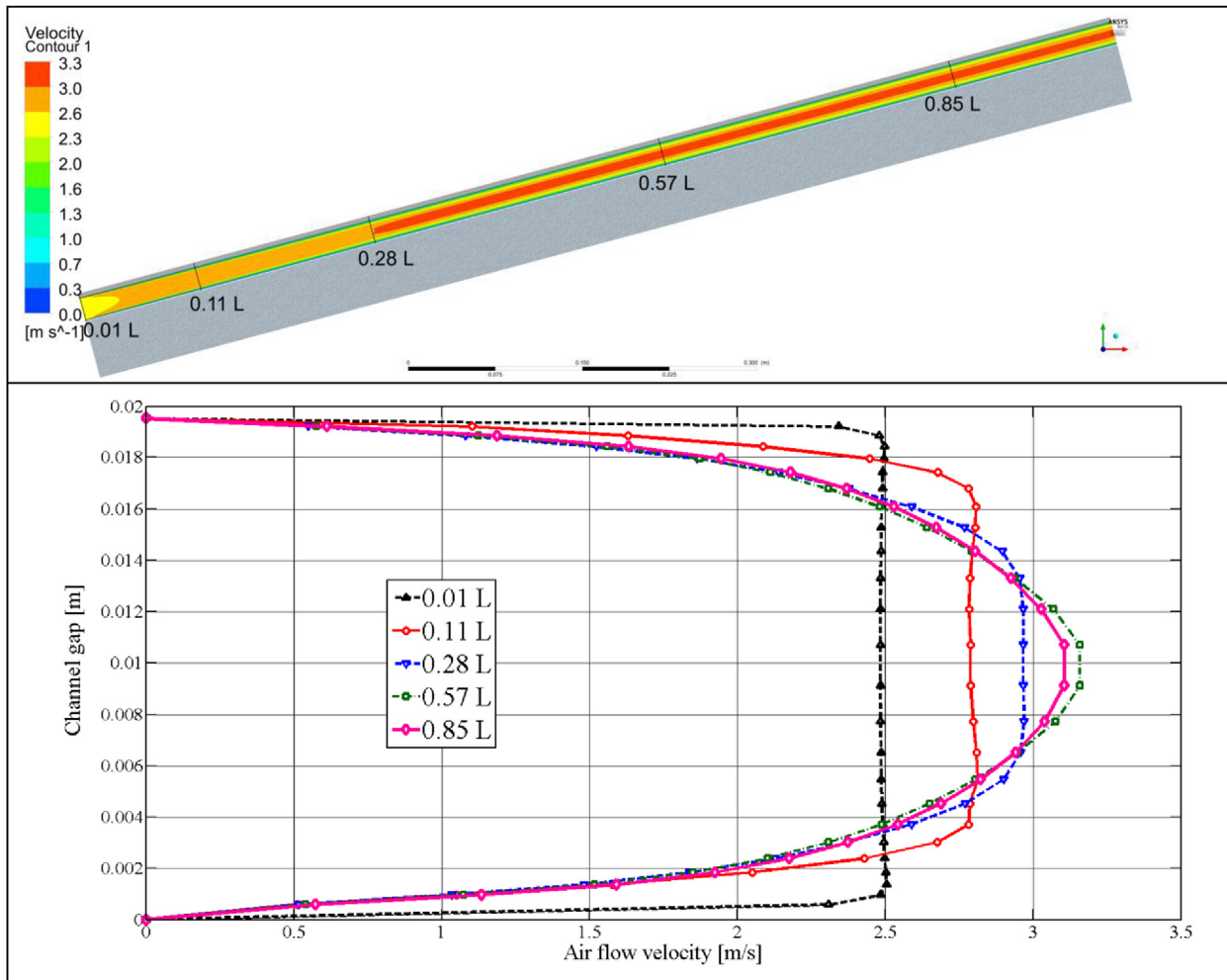


**Fig. 5.** Air velocity contours (top) and velocity profile at several airflow path positions (bottom) of Singh and Kumar's (2012) one-step SAHC:  $I = 800 \text{ W/m}^2$ ,  $T_{\text{amb}} = 30.07^\circ\text{C}$  and  $\dot{m}_{\text{air}} = 0.026 \text{ kg/s}$ .

and ambient temperature immediately meets the collector plate, generating high temperature gradients between the air and the collector plate. The collector plate temperature will then gradually reduce throughout the solar collector as a result of the continuous air heating by the collector plate.

On the other hand, the lower graph in Fig. 7 shows that the glass cover presents no significant variation to the surface temperature along the collector. Only a variation of  $1.8^\circ\text{C}$  in the minimum and maximum temperature of the glass cover can be observed. It should also be noted that these temperatures are not high when they are compared to the ambient temperature, which is presumed to be due to the low absorbance that was assigned in the simulations for the glass cover. Prior knowledge of this property allows us to obtain results with a higher level of confidence.

Fig. 8 shows the quantitative results of the radiant, convective and total external surface fluxes of the collector plate in the condition of maximum irradiance and maximum air mass flow rate. It is worth noting that, according to the conventions used by the software in the energy balance over a control surface, the negative sign indicates that the heat flux enters the collector plate-air boundary surface. Conversely, the positive sign indicates that the heat flux leaves the collector plate-air boundary surface.

Thus, according to the quantitative results of Fig. 8, the radiant heat flux is not uniform. The radiant heat flux is higher in regions of air inlet, where it reaches peak values near  $500 \text{ W/m}^2$ , which

means that 62.5% of solar irradiation enters the collector plate-air boundary surface. This maximum radiant heat flux then slowly decreases along the collector plate to values close to  $420 \text{ W/m}^2$  (or 52.5% of  $I$ ) in almost all the airflow path.

This behaviour can be explained by Eq. (13), where the radiant heat flux is the result of competition between the incident energy fraction from the sun absorbed by the collector plate and the energy emitted by the plate surface. Because the surface temperature of the collector plate is low at the beginning of the air duct, the emitted radiant energy will also be low because, at the same irradiation, the radiative heat flux will increase as the surface plate temperature increases.

Much of the net radiant energy is transferred to the air through convection phenomena. Thus, as is shown in Fig. 8, the convective heat flux, which transfers the collecting plate to the air, is greater than  $400 \text{ W/m}^2$  in the first 40 mm of the airflow path. However, as its route continues, the convective heat flux tends to slowly decrease until it settles down to values around  $320 \text{ W/m}^2$  in the region of the collector plate near the air exit. This decreasing behaviour of the convective heat flux is attributed to the monotonic decrease in the temperature difference between the collector plate surface and the adjacent air region.

Finally, the total heat flux corresponds to the algebraic sum of the radiant heat flux and the convective heat flux. This parameter indicates where remaining energy is targeted. For the case where

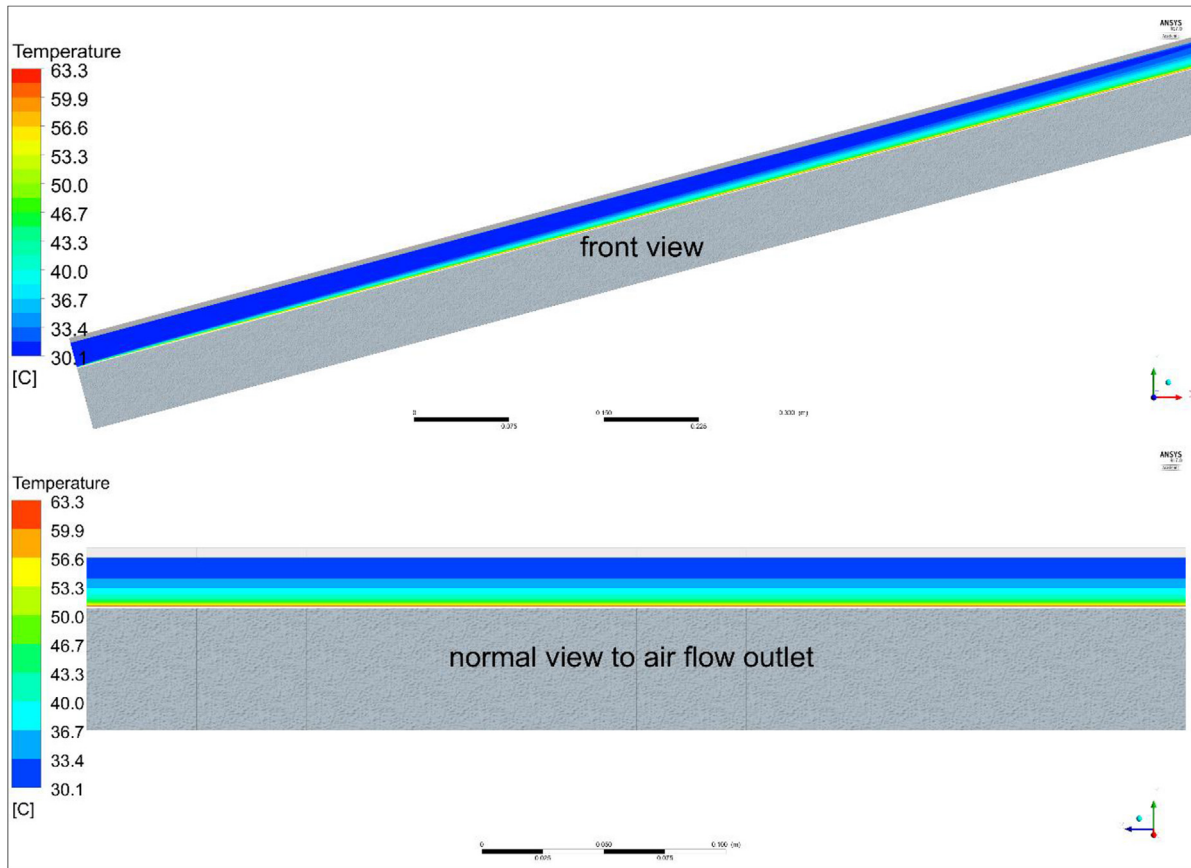


**Fig. 6.** Air temperature contours inside the solar collector for  $I = 800 \text{ W/m}^2$ ,  $T_{\text{amb}} = 30.07^\circ\text{C}$  and  $\dot{m}_{\text{air}} = 0.026 \text{ kg/s}$ .

the total heat flux is in a negative form, this indicates that a fraction of radiant energy that has not been transferred to the air through convection is transferred to the insulator via thermal conduction.

Nevertheless, as can also be seen in Fig. 8, the total heat flux in the first 20 mm of length of the collector plate is positive. Under this condition, the convective heat transfer is greater than the thermal radiation transfer. This situation happens when an “extra” heat flux comes from another thermal energy source. As shown in Fig. 7, the gradient temperature in the collector plate generates a conduction heat flux that travels from upstream to downstream. Thus, the convective heat transfer in the first 20 mm of the collector’s length is the result of the heat fluxes stemming from thermal radiance and thermal diffusion.

### 3.3. Comparative study of three solar collectors working under the same operating conditions

In this section, the CFD simulation results from three different configurations of SAHCs are presented and discussed in order to identify the SAHC that delivered the best thermal performance under the same operating conditions. The SAHCs’ geometries in analysis include the following:

- The one-step SAHC of Singh and Kumar (2012), which was previously discussed in the preceding sections (see Fig. 2);
- The three-step A-type SAHC, whose collector plate is attached to the insulator base in the lowest channel (see Fig. 9a); and
- The three-step B-type SAHC, where the collector plate delimits the intermediary channel’s lower region and the upper region of the lower channel (see Fig. 9b).

It is worth emphasising that the three SAHCs have the same sun exposure area of 0.92 m in length and 0.45 m in width, and the same distance, 0.02 m, between the channels where air flows into the collector. The materials are also the same for the three solar collectors.

The three SAHCs were subjected to a condition in which the air at a room temperature of  $30.07^\circ\text{C}$  entered the collector with a mass flow of  $0.009 \text{ kg/s}$ , while the sun irradiated  $800 \text{ W/m}^2$  on the upper outer surface of the collector delimited by the glass cover.

Fig. 10 shows the contours of the air temperature circulating inside the three SAHCs. It can be seen that, in the case of the one-step SAHC, the air presents elevated temperatures in the near region of the collector plate region whereas, in the neighbouring region to the collector plate region, temperatures are slightly higher than the air temperature. This behaviour is due to the existing high temperature between the glass cover and the collector plate, which is characteristic of this type of collector.

In the case of the three-step A-type SAHC, it can be noted that the air temperature hardly increases in the first two run channels. This is because temperatures glasses delimiting such channels are too low in a way that the convection heat transfer is almost negligible.

However, when the air enters the third channel it meets the collector plate so that the heat transfer becomes more effective. Note that the temperature air gradients in a normal direction to the channel are smaller than in the case of the one-step SAHC because (i) airflow transitions from one channel to the next, generating swirls in the normal direction to the plates, which in turn generate a turbulent diffusion of thermal energy that uniformises the air temperature in the regions near those transitions; (ii) the jump of

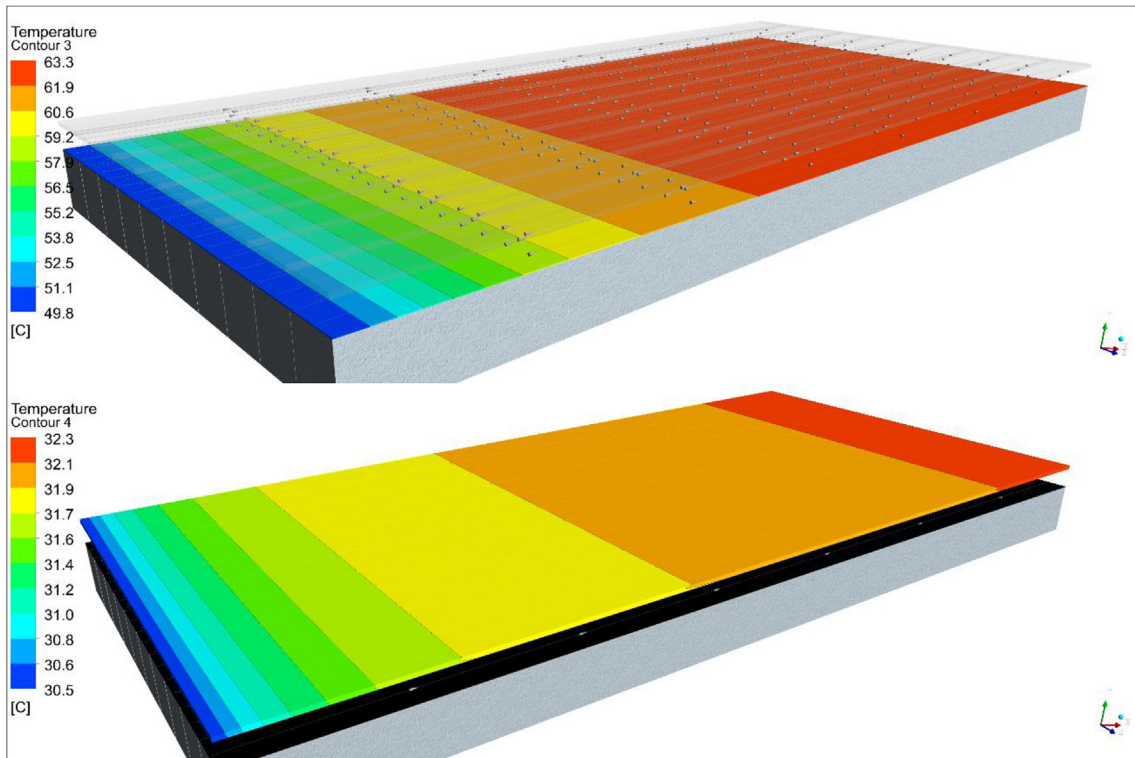


**Fig. 7.** Surface temperatures of the collector plate (top) and solar collector cover (bottom):  $I = 800 \text{ W/m}^2$ ,  $T_{\text{amb}} = 30.07 \text{ }^{\circ}\text{C}$  and  $\dot{m}_{\text{air}} = 0.026 \text{ kg/s}$ .

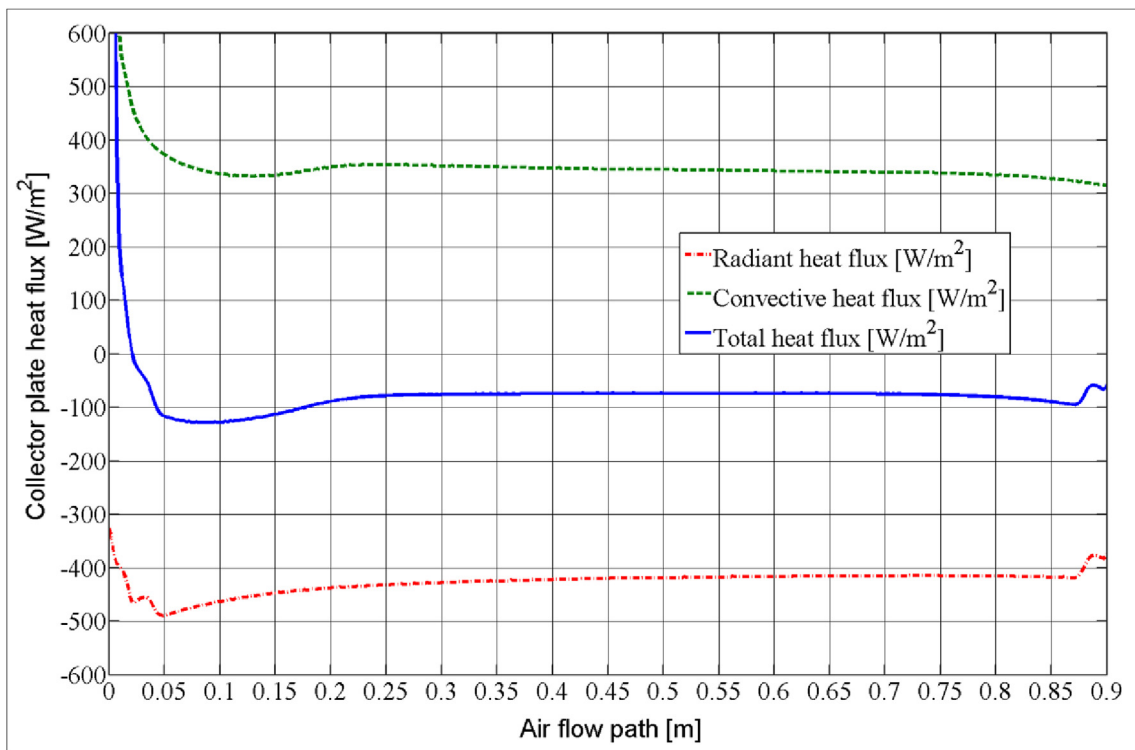


**Fig. 8.** Radiant and convective heat flux in the interface air/collector plate for  $I = 800 \text{ W/m}^2$ ,  $T_{\text{amb}} = 30.07 \text{ }^{\circ}\text{C}$  and  $\dot{m}_{\text{air}} = 0.026 \text{ kg/s}$ .

temperature in the third channel is smaller than in the case of the one-step SAHC due to the attenuation of radiant thermal energy from the three glasses; and (iii) the air temperature that enters the

third channel is greater than the ambient temperature because, in the first two channels, the glasses have previously transferred to the air, part but not significant of its thermal energy resulting from

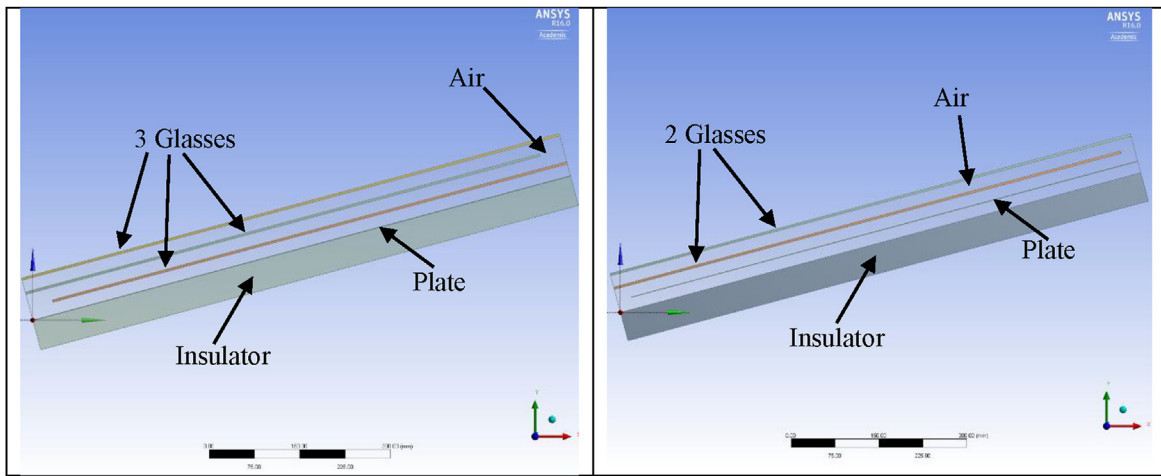


**Fig. 9.** Geometric configuration of two three-step SAHCs: (a) A-type (left) and (b) B-type (right).

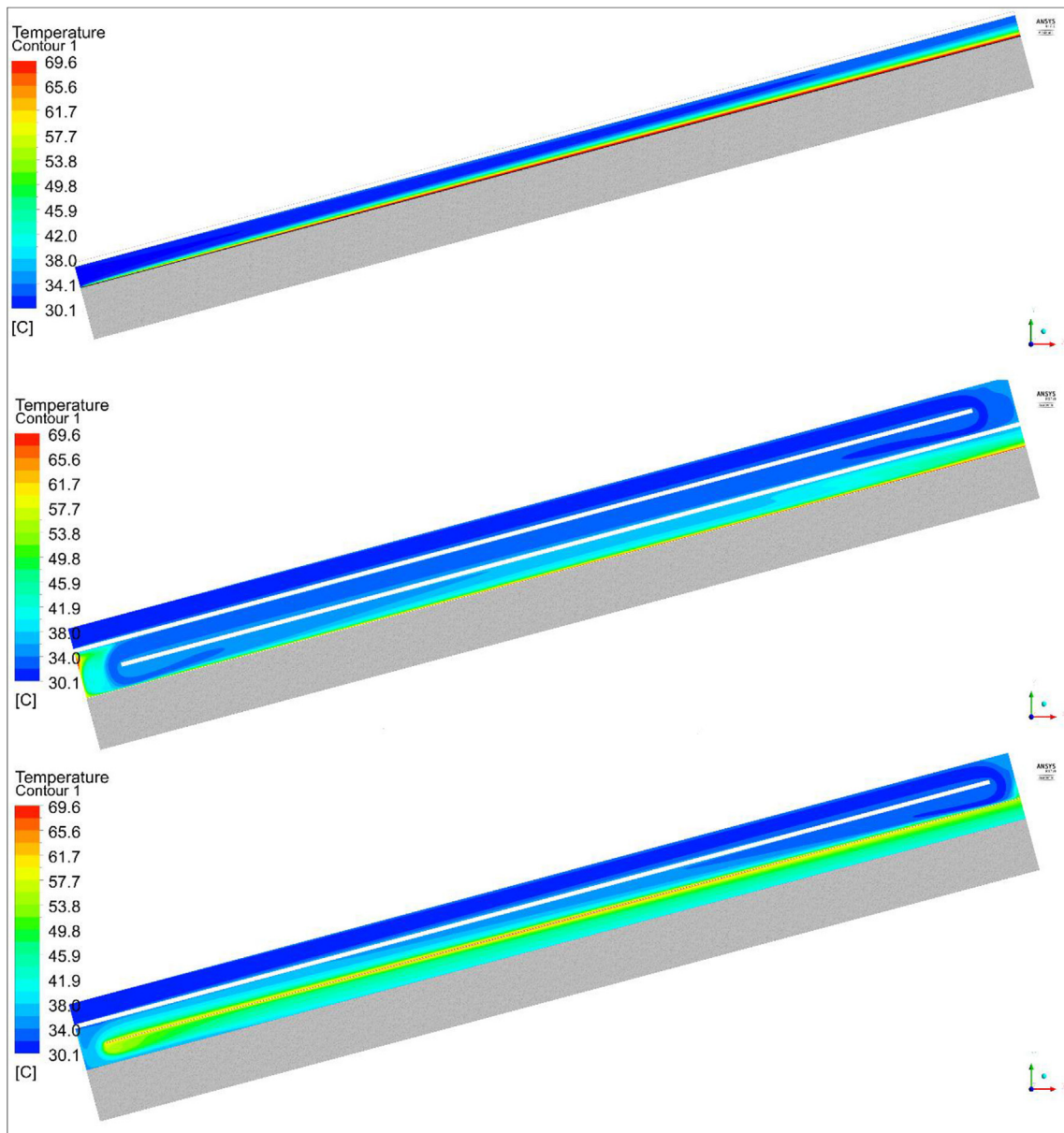


**Fig. 10.** Internal air temperature contours in the operation of SAHCs: one-step (above) and three-step A-type (centre) and B-type (below):  $I = 800 \text{ W/m}^2$ ,  $T_{\text{amb}} = 30.07^\circ\text{C}$  and  $\dot{m}_{\text{air}} = 0.009 \text{ kg/s}$ .

their low absorption.

As shown in Fig. 10, in the case of the three-step B-type collector the air flows inside of this device with temperatures that are more homogeneous than previous SAHCs. This is mainly due to the fact that the air exposure surface with the collector plate is higher than in the previous cases. This, coupled with the channel transitions of three-step SAHCs, allows turbulent diffusion in the same way, as there is no physical contact between the collector plate and the insulation material. The last situation makes the air facing the solar collector absorb more heat energy, reducing the thermal energy losses that occur by conduction between the collector plate and the insulating material.

The quantitative results of the main thermal parameters for the three SAHCs analysed are shown in Table 4 and Fig. 11. These representations demonstrate that the outlet air temperature for the three-step B-type SAHC is 5.5 °C greater than in the case of the one-step SAHC. This last SAHC is, in turn, 2.2 °C lower than the three-step A-type SAHC. This gain in air temperature in the case of the three-step B-type SAHC is the result of the increased absorption of

thermal energy where, under the same operating conditions, the collector absorbs 63 W more than that absorbed by the one-step SAHC, which is equivalent to an increase of 67% of the thermal power. Of course, the thermal efficiency of the collector of the three-step B-type SAHC is also higher than the one-step SAHC, in the same proportion as the thermal energy absorbed by the air. Finally, the average temperature of the collector of the three-step B-type SAHC is almost 15 °C lower than that of the one-step SAHC.

#### 4. Conclusion

This research aimed to validate a model based on CFD in order to apply the model to the design and analysis of high efficiency SAHCs that are able to meet the thermal requirements necessary for drying cocoa beans in the shortest time possible. Following this, a parametric study of three different types of SAHCs operating at equal conditions was completed, with the aim of choosing the geometric configuration that ensures the highest thermal performance. Using the results and discussions from these activities, the following conclusions were reached:

- The CFD model developed here was successfully validated through comparison with the experimental measurements of Singh and Kumar (2012) concerning the operation of a one-step SAHC, where discrepancies less than 6% were reported for the air temperature at the outlet of such equipment.
- The use of the CFD model for the simulation of three SAHCs showed that the three-step B-type SAHC demonstrated the best

**Table 4**

The numerical values of mass averaged outlet air temperature,  $T_{air,exit}$ , area averaged collector plate temperature,  $T_{plate}$ , absorbed thermal power,  $\dot{Q}_{abs}$ , and thermal efficiency,  $\eta_T$ , for the one-step, three-step A- and B-type SAHCs.

SAHC type	$T_{air,exit}$ [°C]	$T_{plate}$ [°C]	$\dot{Q}_{abs}$ [W]	$\eta_T$ [%]
One-step	41.9	78.0	94	28.4
Three-step type A	44.1	65.2	127	38.2
Three-step type B	47.4	63.4	157	47.4

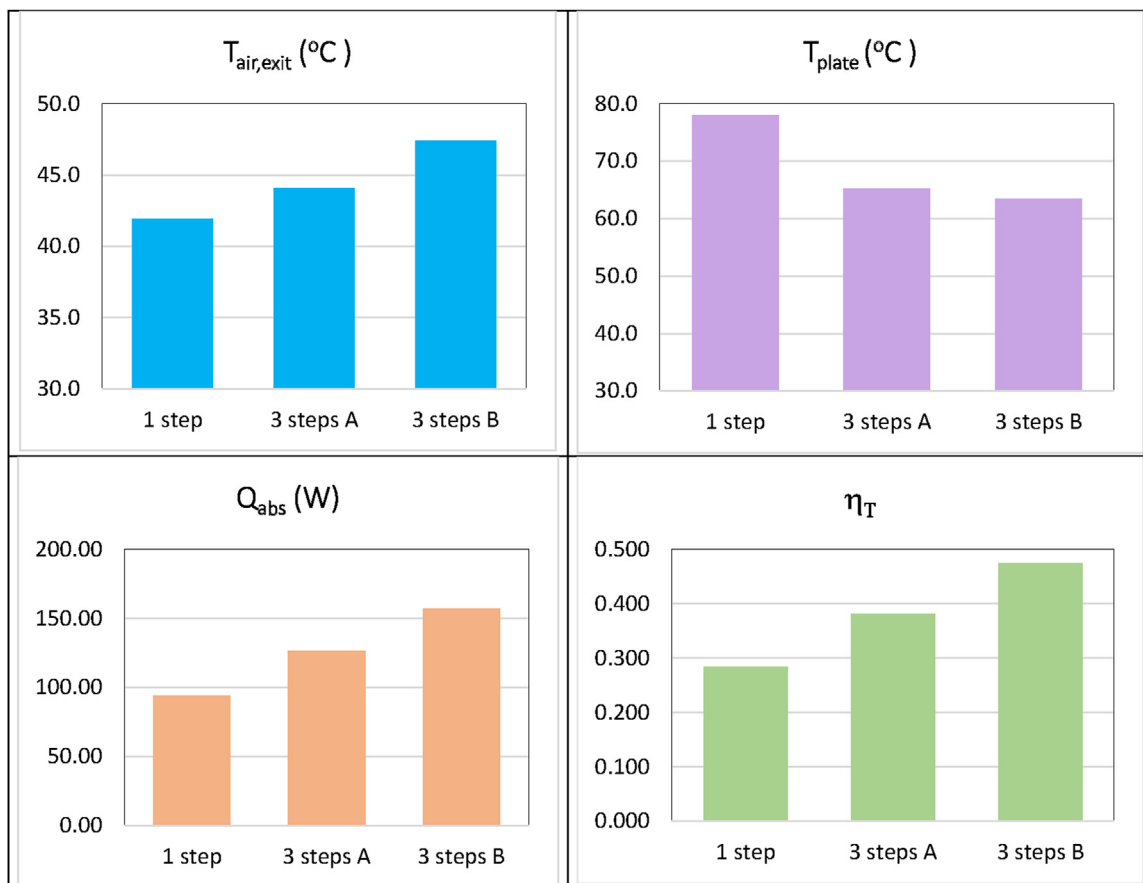


**Fig. 11.** Comparative graphs of the air temperature at the outlet,  $T_{air,exit}$ , temperature of the collector plate,  $T_{plate}$ , absorbed thermal power,  $\dot{Q}_{abs}$ , and thermal efficiency,  $\eta_T$ , for the one-step and three-step A- and B-type SAHCs.

thermal performance. This is because the heat transfer rate absorbed by the air in the three-step B-type SAHC was 67% more than that observed in the case of the one-step SAHC.

## Acknowledgements

The authors would like to offer special thanks to the “Fondo Nacional de Desarrollo Científico y Tecnológico – CONCYTEC” for funding the project, “Alianza público privada para el desarrollo de tecnologías que incrementen el valor agregado en las cadenas agroindustriales con énfasis en innovación social y desarrollo sustentable”, by the contract No 013–2014 – FONDECYT.

## References

- Amanlou, Y., Zomorodian, A., 2010. Applying CFD for designing a new fruit cabinet dryer. *J. Food Eng.* 101, 8–15. <http://dx.doi.org/10.1016/j.jfoodeng.2010.06.001>.
- ANSYS, Inc., 2012. ANSYS FLUENT 12.0. Theory Guide.
- Bejan, A., 2013. Convection Heat Transfer, fourth ed. John Wiley and Sons Press, New Jersey.
- Bennamoun, L., Khama, R., Léonard, A., 2015. Convective drying of a single cherry tomato: modeling and experimental study. *Food Bioprod. Process.* 94, 114–123. <http://dx.doi.org/10.1016/j.fbp.2015.02.006>.
- Chandrasekhar, S., 1960. Radiative Transfer, first ed. Dover Publications, New York.
- Chauhan, P.S., Kumar, A., Tekasakul, P., 2015. Applications of software in solar drying systems: a review. *Sustain. Energy Rev.* 51, 1326–1337. <http://dx.doi.org/10.1016/j.rser.2015.07.025>.
- Fudholi, A., Sopian, K., Bakhtyar, B., Gabbasa, M., Othman, M.Y., Ruslan, M.H., 2015. Review of solar drying systems with air based solar collectors in Malaysia. *Renew. Sustain. Energy Rev.* 51, 1191–1204. <http://dx.doi.org/10.1016/j.rser.2015.07.026>.
- Jain, D., Tewari, P., 2015. Performance of indirect through pass natural convective solar crop dryer with phase change thermal energy storage. *Renew. Energy* 80, 244–250. <http://dx.doi.org/10.1016/j.renene.2015.02.012>.
- Kumar, C., Karim, A., Saha, S.C., Joarder, M.U.H., Brown, R., Biswas, D., 2012. Multi-physics modelling of convective drying of food materials. In: Proceedings of the Global Engineering, Science and Technology Conference. Dhaka, Bangladesh.
- Leon, A.M., Kumar, S., 2007. Mathematical modeling and thermal performance analysis of unglazed transpired solar collector. *Sol. Energy* 81, 62–75. <http://dx.doi.org/10.1016/j.solener.2006.06.017>.
- Modest, M.F., 2003. Radiative Heat Transfer, second ed. Academic Press, London.
- Orbegoso, E.M., Figueira da Silva, L.F., Serfaty, R., 2015. Comparative study of thermal radiation properties models in turbulent non-premixed sooting combustion, numerical heat transfer, part a: applications. *Int. J. Comput. Methodol.* 69, 166–179. <http://dx.doi.org/10.1080/10407782.2015.1052318>.
- Peng, D., Zhang, X., Dong, H., Lv, K., 2010. Performance study of a novel solar air collector. *Appl. Therm. Eng.* 30, 2954. <http://dx.doi.org/10.1016/j.applthermeng.2010.07.010>, 2601.
- Schlichting, H., Gersten, K., 2000. Boundary-layer Theory, eighth ed. Springer Verlag, Berlin.
- Singh, S., Kumar, S., 2012. Testing method for thermal performance based rating of various solar dryer designs. *Sol. Energy* 86, 87–98. <http://dx.doi.org/10.1016/j.solener.2011.09.009>.
- Sun, C., Liu, Y., Duan, C., Zenghi, Y., Chang, H., Shu, S., 2016. A mathematical model to investigate on the thermal performance of a flat plate solar air collector and its experimental verification. *Energy Convers. Manag.* 115, 43–51. <http://dx.doi.org/10.1016/j.enconman.2016.02.048>.
- Turner, J.S., 1973. Buoyancy Effects in Fluids, first ed. Cambridge Press, Cambridge.
- VijayaVenkataRaman, S., Iniyar, S., Goic, R., 2012. A review of solar drying technologies. *Renew. Sustain. Energy Rev.* 16, 2652–2670. <http://dx.doi.org/10.1016/j.rser.2012.01.007>.
- Wilcox, D.C., 2008. Formulation of the k-omega turbulence model revisited. *AIAA J.* 46, 2823–2838. <http://dx.doi.org/10.2514/1.36541>.